Understanding and Controlling the Aggregative Growth of Platinum Nanoparticles in Atomic Layer Deposition: an Avenue to Size Selection

Fabio Grillo,* Hao Van Bui, Jacob A. Moulijn, Michiel T. Kreutzer, and J. Ruud van Ommen

Department of Chemical Engineering, Delft University of Technology, 2629 HZ Delft, The Netherlands

E-mail: f.grillo@tudelft.nl

Supporting Information

ALD experiments

The ALD experiments were carried out in a home-built fluidized bed reactor operating at atmospheric pressure as described elsewhere.[1] Briefly, the system consists of a glass column (26 mm in internal diameter and 500 mm in height) placed on top of a single motor Paja PTL 40/40-24 vertical vibration table to assist the fluidization. The graphene nanoplatelets (6-8 nm thick and 12 μm wide, surface area of about 150 m^2 g^{-1}, see Fig. S1 b.) and the trimethyl (methylcyclopentadienyl)platinum(IV) (MeCpPtMe3) precursor were obtained from Strem Chemicals and used as received. Synthetic air (20 wt % oxygen) was used as the oxidizer. The Pt precursor, contained in a stainless steel bubbler, was heated and maintained at 70 °C, whereas the stainless steel tubes connecting the bubbler and the reactor were maintained at 80 °C to avoid precursor condensation. The reactor was heated by an infrared lamp placed parallel to the column with feedback control to maintain a constant temperature during ALD. In each experiment, 0.75 g of graphene powder was used. A gas flow of 0.5 L min-1 was introduced through a distributor plate at the bottom of the reactor column in order to fluidize the powders. Prior to ALD, the powders were dried in air at 120 °C for 1 h. Thereafter, an ozone treatment step at 200 °C for 30 min was applied, which was performed by flowing synthetic air (0.5 L min^{-1}) through an OAS Topzone ozone generator. The ozone-enriched air thus obtained had an ozone content of about 1.5 wt %. The ALD process consisted of sequential exposures of the powders to the Pt precursor (4 min) and synthetic air (5-10 min), separated by a purging step (5 min) using nitrogen as an inert gas (N2, 99.999 vol%).

Raman spectroscopy

The Raman spectra were acquired using a Renishaw inVia Raman microscope equipped with a 514 nm excitation laser. The Pt/graphene powders were immobilized on monocrystalline Si wafers. The Raman peak of Si substrate at 520 cm^{-1} was used as the reference for the Pt/graphene peak position calibration in each measurement. The Raman spectra were measured in air with a 20 mW laser power. The integration time for all Raman spectra was 100 ms. The scanned range was 500-3500 cm^{-1} with intervals of 1.5 cm^{-1}.

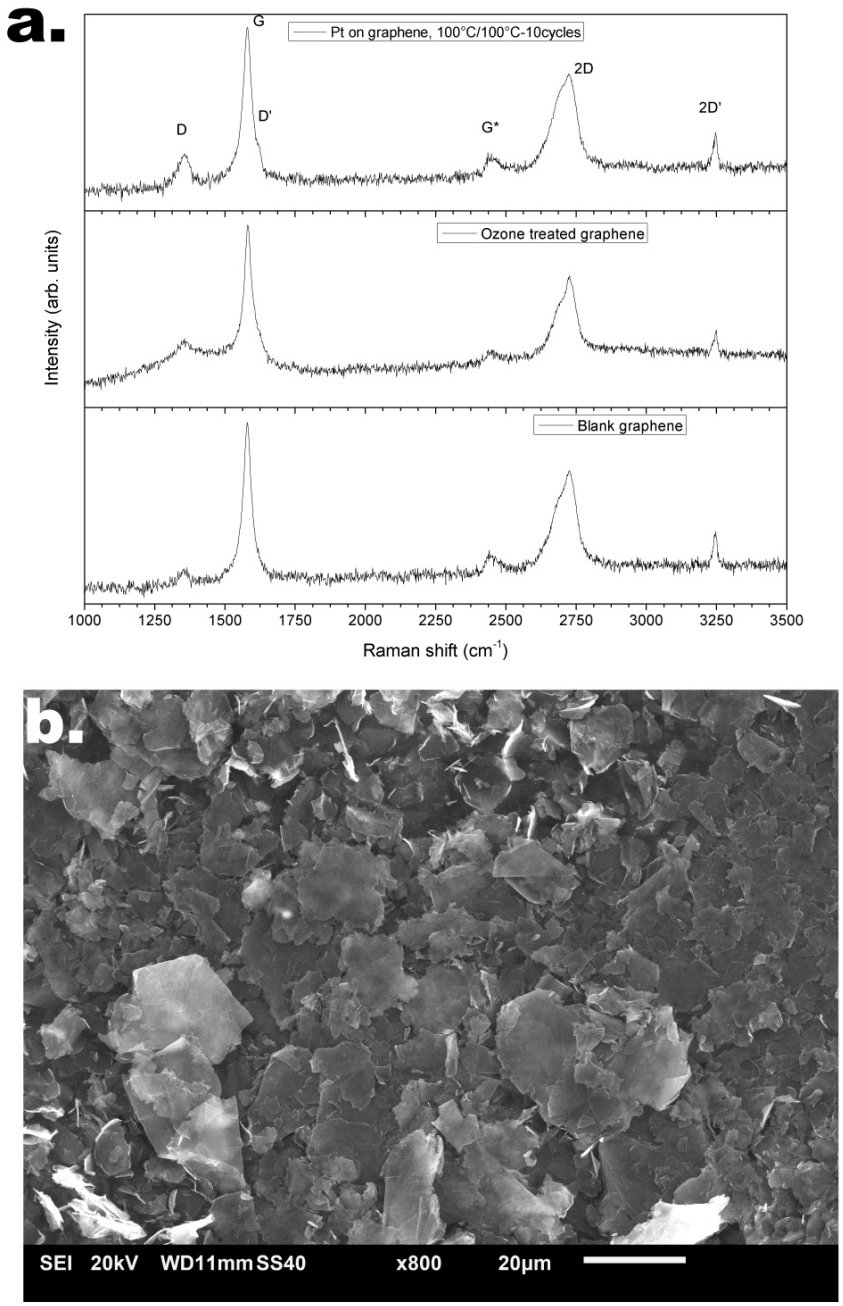

Figure S1: (a) Raman spectra obtained for blank graphene nanoplatelets, Ozone-treated graphene nanoplatelets, and Ozone-treated graphene nanoplatelets after 10 ALD cycles at 100°C. The spectrum for the blank sample is consistent with few-layer defective graphene. The ozone treatment resulted in a slight increase D peak height, suggesting an increase in the defect density consistent with the incorporation of oxygen-containing species. 10 ALD cycles resulted in the appearance of the D' peak, which is also a signature of the presence of defects, and in the accentuation of the D peak, which might be due to the incorporation of Pt NP. Analogous trends were found for all the deposition temperatures considered here. (b) SEM micrograph of the blank graphene nanoplatelets.

X-ray Photoelectron spectroscopy (XPS)

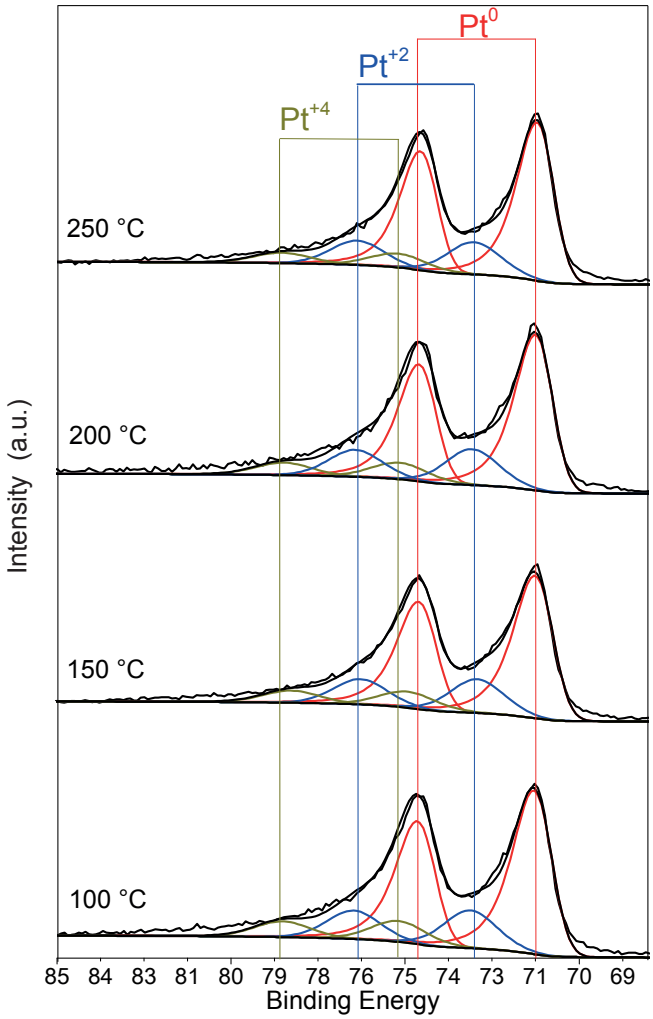

Figure S2: Pt $4f$ XPS spectra obtained for the Pt deposited on graphene nanoplatelets after 10 ALD cycles at 100 °C, 150 °C, 200 °C, and 250 °C. The binding energies were calibrated using the C1s peak at 284.5 eV as a reference. Before peak fitting, the background was estimated and subtracted by using a Shirley background type. The Pt $4f$ fits were obtained by fixing the separation between $4f_{7/2}$ and $4f_{5/2}$ peaks to the theoretical value of $\sim$ 3.3eV and the ratio between the areas of $4f_{7/2}$ and $4f_{5/2}$ peaks equal to theoretical value of $\sim 4/3$. The full width at half maximum (FWHM) values were kept constant for all the spectra and equal to about 1.2 eV, 1.8 eV, and 1.9 eV for the Pt^0, Pt^{+2}, and Pt^{+4} peaks, respectively. The spectra were fitted by using 3 doublets, namely, two asymmetric Gaussian-Lorentzian line-shapes with an asymmetric index equal to 0.2 for metallic platinum and two Gaussian-Lorentz line-shapes for both Pt^{+2}, and Pt^{+4}. By doing so, the positions of the Pt $4f_{7/2}$ peaks were found to be $\sim$71, $\sim$73.1 and $\sim$75.2, in agreement with the values reported in literature. Metallic platinum accounted for more than 70% of the atomic concentration of platinum species in all temperature cases. The presence of Pt^{+2} and Pt^{+4} peaks is ascribable to the omnipresent PtO_x species and in particular PtO, Pt(OH), and PtO_2 on the surface of Pt NPs. In particular, Pt^{+2} and Pt^{+4} accounted for about 20% and 10%, respectively, of the deposited platinum.

X-ray Powder Diffraction (XRD)

The Pt/graphene was transferred onto a Si wafer with 300 nm of SiO2 thermal oxide. This was to eliminate the influence of the substrate (Si) signal in the XRD patterns of the powders. XRD patterns were obtained by a PANalytical X-pert Pro diffractometer with Cu Kα radiation, secondary flat crystal monochromator and X'celerator RTMS Detector system. The angle of interest 2θ was measured from 10° to 90° with fine steps of 0.001°.

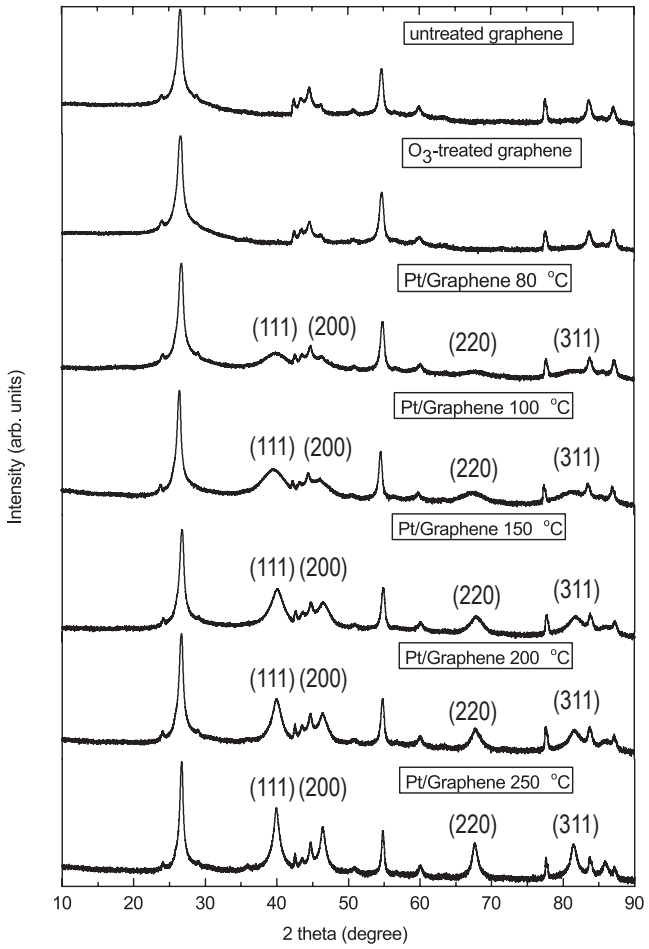

Figure S3: XRD spectra obtained for untreated graphene nanoplatelets, ozone-treated graphene nanoplatelets, and Pt deposited on ozone-treated graphene nanoplatelets after 10 cycles at 80 °C, 100 °C, 150 °C, 200 °C, and 250 °C. The ozone treatment had little to no effect on the graphene powders crystallinity. The signature of metallic Platinum is present at all deposition temperatures considered here. In particular, the peaks corresponding to metallic platinum consistently sharpens with increasing deposition temperatures, which is consistent with the increased frequency of large NPs ($d_p >$ 5 nm) at deposition temperatures above 100 °C (see S5, S6, S7, and S8).

Transmission Electron Microscopy (TEM) and High Resolution TEM (HRTEM)

As-synthesized Pt/graphene powders were suspended in ethanol and transferred to regular transmission electron microscopy (TEM) grids (3.05 mm in diameter). High resolution TEM (HRTEM) micrographs were obtained using a FEI Titan G2 60-300 transmission electron microscope operated at 300 kV. TEM images were taken at several locations on the grids using a JEOL JEM1400 transmission electron microscope operating at a voltage of 120 kV and a current density of 50 pA cm^{-2}. The images were then analyzed by using the ImageJ software to obtain the PSDs. More than 6000 particles were analyzed for each PSD (see Fig. S4).

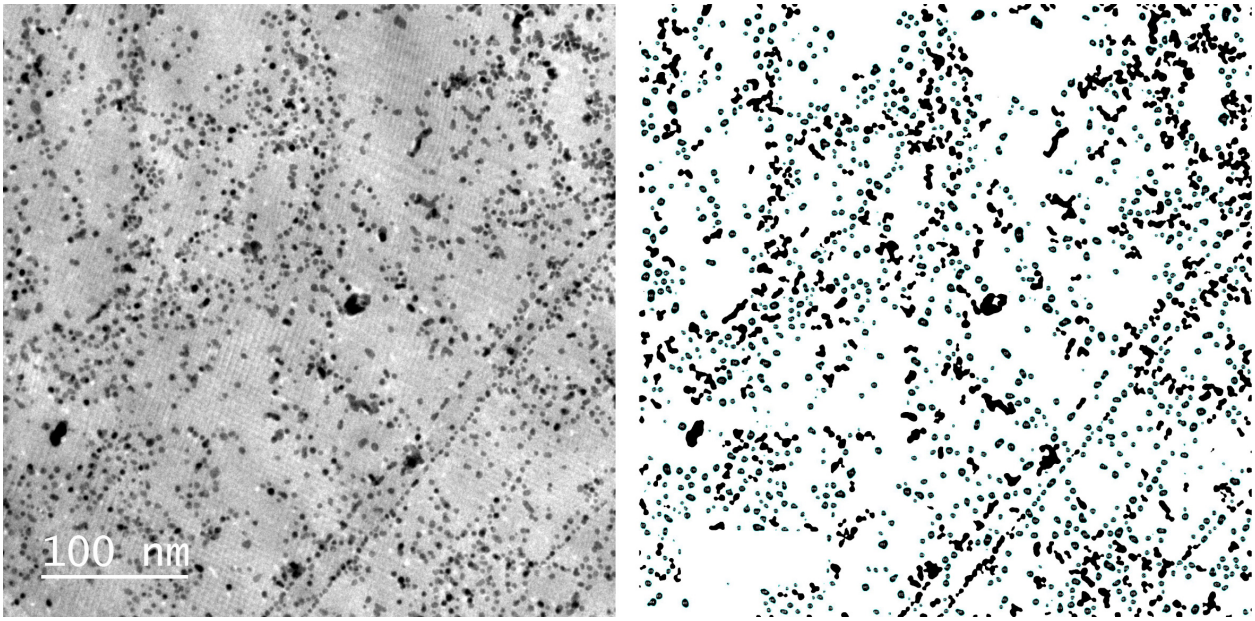

Figure S4: Example of TEM micrograph before and after image analysis. The image analysis was performed via the software ImageJ in a semi-automatic fashion and consisted of several steps, including, background subtraction, Fast Fourier Transform (FFT) bandpass filtering, thresholding, and segmentation via edge detection. For the particle analysis the edge detection algorithm was allowed to detect objects with circularity between 0.85 and 1 to account for those nanoparticles whose 2D projection was not perfectly circular.

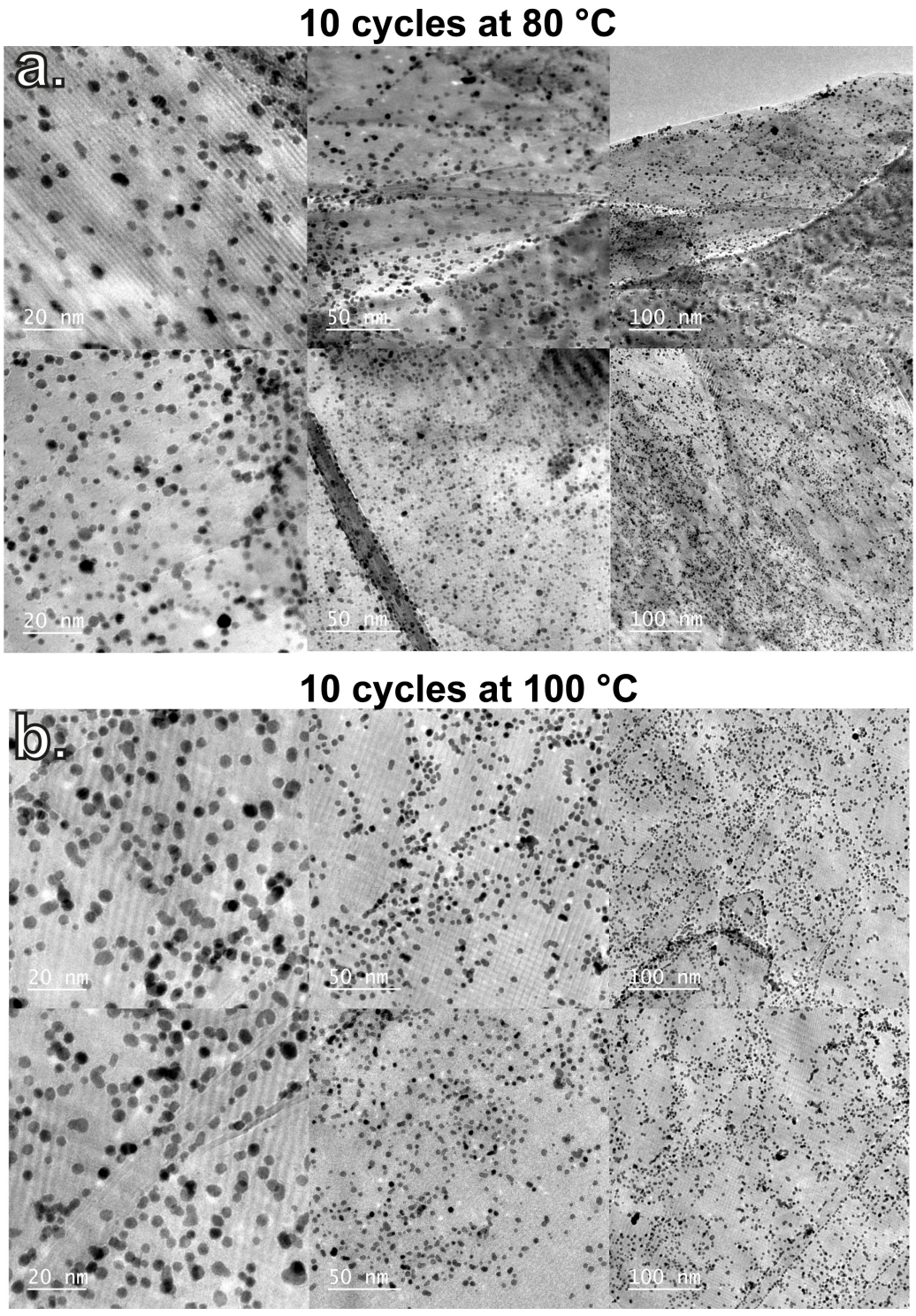

Figure S5: TEM micrographs of Pt deposited on graphene nanoplatelets after 10 cycles at 80 °C (a) and 100 °C (b), taken at different magnifications.

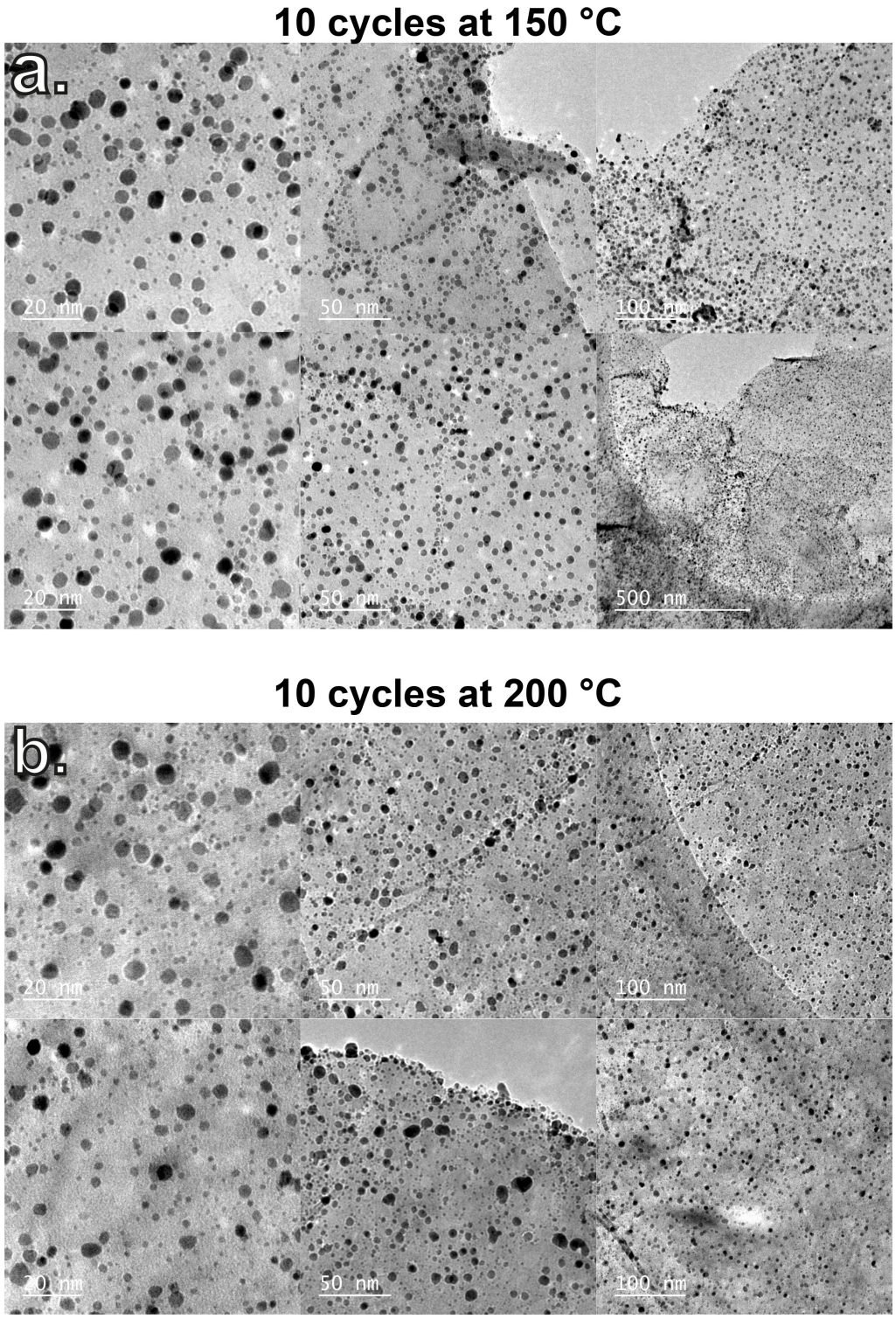

Figure S6: TEM micrographs of Pt deposited on graphene nanoplatelets after 10 cycles at 150 °C (a) and 200 °C (b), taken at different magnifications.

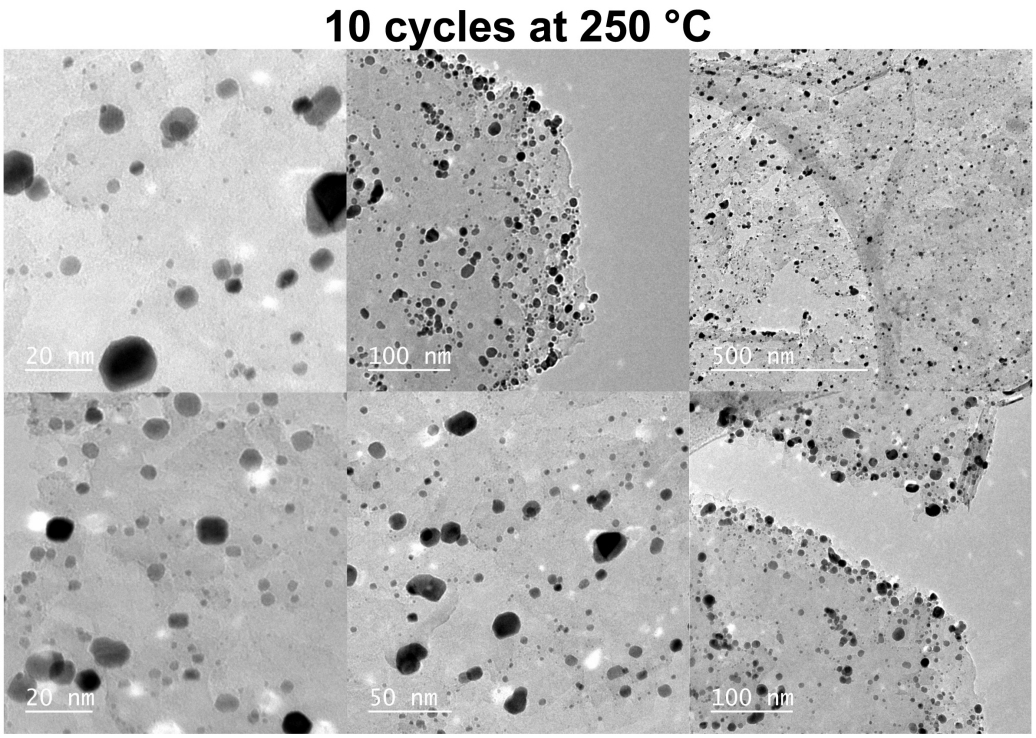

Figure S7: TEM micrographs of Pt deposited on graphene nanoplatelets after 10 cycles at 250 °C taken at different magnifications.

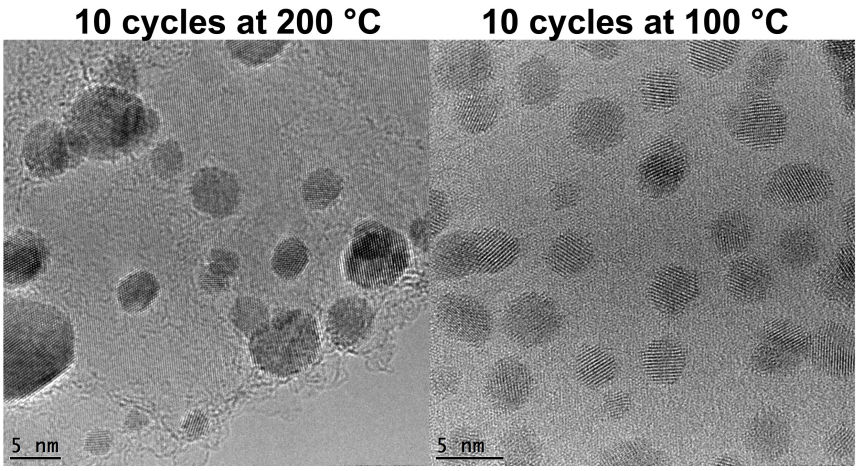

Figure S8: HRTEMs micrographs of Pt deposited on graphene nanoplatelets after 10 cycles at 200 °C and 100 °C.

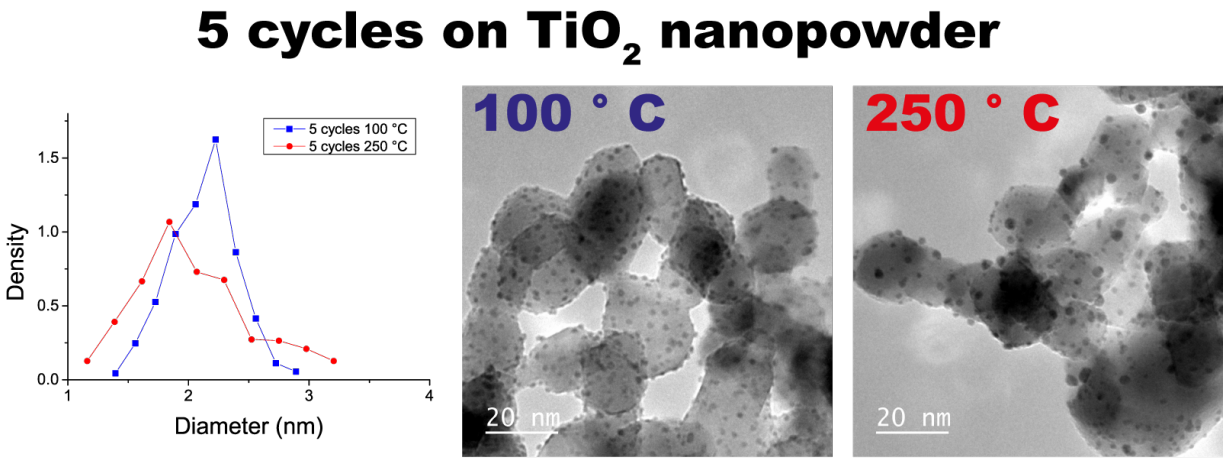

Figure S9: Representative TEMs micrographs of Pt NPs deposited on Degussa P-25 TiO_2 nanoparticles (50 m^2 g^{-1}, $d_p = 21$ nm) after 5 cycles at 100 °C and 250 °C (1.5 g of powder per batch, time scheme: 5 min/5 min/5 min /5 min), and the respective PSDs (each PSD was estimated by analyzing more than 400 particles in several micrographs).

Loading vs PSD

The platinum loading (wt%) was measured via Instrumental Neutron Activation Analysis(INAA). INAA was carried out at the Reactor Institute of Delft (Delft University of Technology). The powders (about 30 mg for each Pt/graphene sample) were loaded into high purity polyethylene capsules. The samples and a standard sample (reference) were then packaged and irradiated in a suitable reactor at a constant neutron flux. All reactors used for neutron activation employed uranium fission, which provides a neutron flux in the order of 1012 cm^{-2} s^{-1}. These neutrons have low kinetic energy, typically less than 0.5 eV. Upon irradiation, a neutron can be absorbed by the target nucleus (i.e., Pt), forming a radioactive nucleus, which carries its own half-life characteristics. The nuclear decay of the radioactive nuclei produce gamma-rays, which are detected by the NAA detectors, from which the Pt loading was determined. For Pt/graphene samples, an average waiting time of 5 days was required to allow the decay of radioactive nuclei. The INAA used in this work allowed detection levels for platinum in the range 101-102 nanograms.

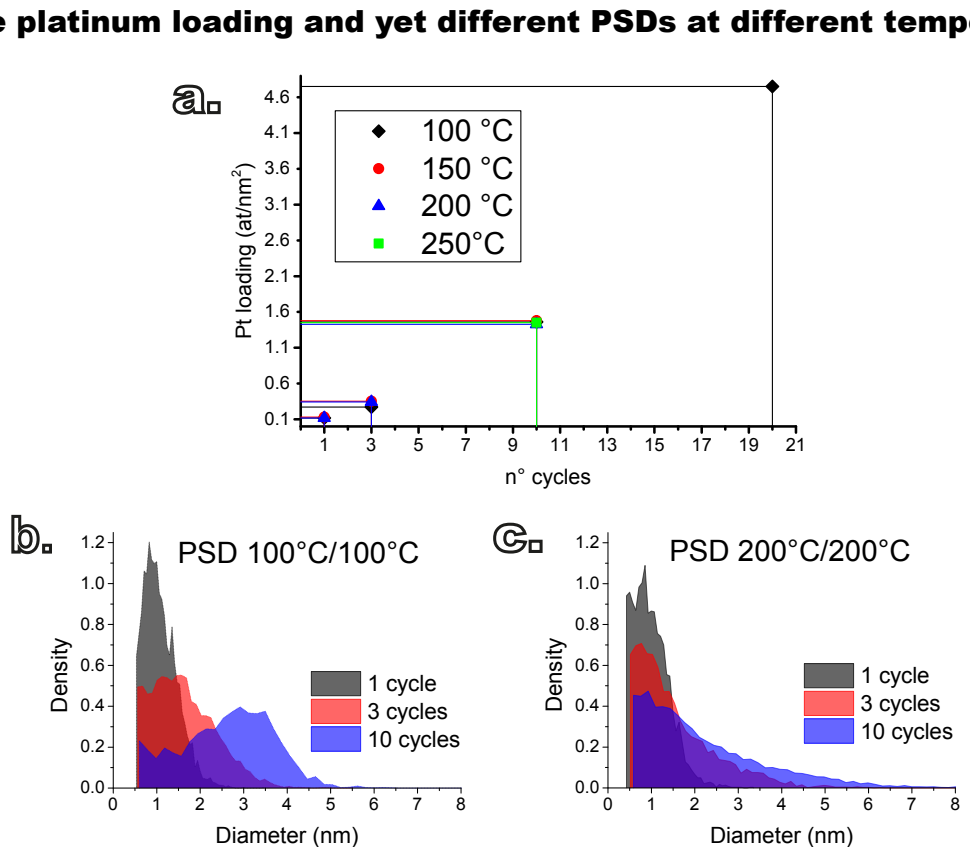

Figure S10: (a) evolution of the Pt loading with the number of cycles at different deposition temperatures (the loading was expressed in terms of at/nm^2 by using Eq. (1= and the Pt weight fraction as obtained via INAA). (b) PSDs after 1,3, and 10 cycles at 100 °C and (c) 200 °C.

Table S1: Platinum loading, NP density, and mean diameter and standard deviation after 1,3, and 10 ALD cycles at 100°C, 150°C, and 200°C.

	100 °C			150°C			200°C		
N° cycles	1	3	10	1	3	10	1	3	10
Pt loading [wt%]	0.51	1.37	6.00	0.57	1.52	6.07	0.51	1.47	5.87
Pt loading [at/nm^2]	0.12	0.31	1.46	0.13	0.35	1.48	0.12	0.34	1.43
NP density [nm^{-2}]	0.0022	0.0019	0.0028	0.0040	0.0020	0.0025	0.0016	0.0028	0.0031
Mean diameter [nm]	1.1	1.6	2.6	1.0	1.54	2.2	1.2	1.3	2.0
Standard deviation [nm]	0.4	0.7	1	0.4	0.9	1.5	0.6	0.8	1.4

The platinum loading after the p-th cycle $G_{tot}(p)$ expressed in terms of at/nm^2 was calculated by using the following expression:[1,2]

$$G_{tot}(p) = \frac{w_p(N_A/A_r)}{(1-w_p)S} \tag{1}$$

where w_p is the weight fraction of Pt in the sample, N_A is the Avogadro constant, A_r is the relative atomic mass of Pt, and S is the surface area per unit weight of the substrate.
The average number of NPs per unit area (NP density) was estimated by assuming the Pt NPs to be metallic close-packed FCC structures. Hence, by geometric construction, the number of atoms N_{atoms} in a Pt NP is given by:[3–5]

$$N_{atoms} = \frac{1}{3}\left[10n^3 - 15n^2 + 11n - 3\right], \; n \geq 1 \tag{2}$$

where n is the number of atomic layers making up the NP, where atomic layer is defined such that when, for example, n is equal to 1 the NP consists of a single atom or central site, whereas when n is equal to 2 the the NP consists of a central site fully coordinated by 12 surface atoms, that is an NP of 13 atoms. The diameter of such NP scales linearly with n according to the following formula:[3]

$$d = (2n-1)a/\sqrt{2} \tag{3}$$

where a is the lattice constant. Therefore, given the normalized PSD $f_p(d)$, we estimated the NP density s_p, by imposing the following mass balance:[1]

$$s_p \int_{d_{min}}^{d_{max}} f_p(x) N_{atoms}(x) dx = \frac{w_p(N_A/A_r)}{(1-w_p)S} \tag{4}$$

The integral in left-hand side of Eq. (4) is the average number of atoms contained in the Pt NPs, which then multiplied by the NP density gives the Pt loading expressed in atoms per unit area, which is given by 1 (right-hand side of Eq. (4)).

Saturation and Thermogravimetric analysis (TGA)

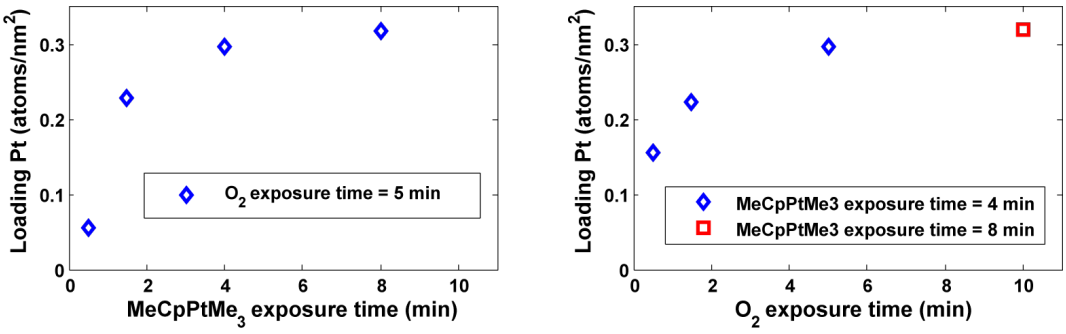

Figure S11: Saturation curves obtained for Pt ALD at 100 °C after 3 cycles on 0.75 g of graphene nanoplatelets with a surface area of 150 m^2 g^{-1}.

A Mettler Toledo TGA/SDTA 851e thermogravimetric analyzer was used for studying the thermal behavior of the synthesized powders. 3 mg of Pt/graphene was used for each TGA measurement. The TGA curves were recorded while ramping up the powders from 25 to 800 °C with a ramping rate of 5 °C min^{-1} in a synthetic air flow of 100 mL min^{-1}.

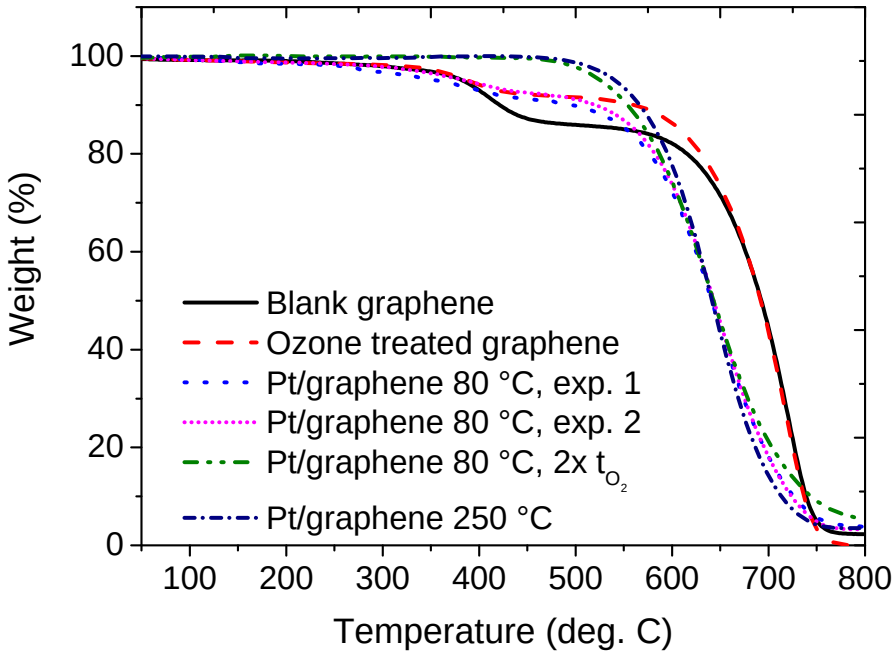

Figure S12: TGA of untreated graphene nanoplatelets before and after the ozone-treatment, and of the ozone-treated graphene nanoplatelets after: 10 cycles at 80 °C, with the exposure time to synthetic air was fixed to either 5 min (two different experiments) or 10 min, and after 10 cycles at 250 °C with the exposure time to synthetic air fixed to 5 min. The shift to lower temperatures of the onset of mass loss of the Pt/graphene composites as compared with the blank graphene is ascribable to the catalytic nature of Pt towards the combustion of carbon. The decreased mass loss in the 400-500 °C temperature range of the ozone-treated graphene nanoplatelets as compared with the TGA of the untreated shows how the ozone treatment effectively removes most of the adventitious carbon adsorbed on the surface of the graphene. Increasing the exposure time to synthetic air to 10 min in the ALD recipe resulted in a removal of carbon ligands comparable to the one obtained at 250 °C with an exposure time of 5 min. This is ascribable to slower combustion kinetics at low temperatures. Pt/graphene obtained at 150 °C and 200 °C with an oxygen exposure of 5 min exhibited the same weight loss profile as Pt/graphene obtained at 250 °C with the same exposure (not shown). Accordingly, an oxygen exposure time of 10 min and 5 min were chosen for the ALD experiments carried out at low temperatures (i.e., 80 °C and 100 °C) and at high temperatures (i.e., 150 °C, 200 °C, and 250 °C), respectively, to assure the same degree of removal of carbon ligands at both low and high temperatures.

Annealing experiments

The annealing of Pt/graphene was carried out in either air or argon atmosphere. For each experiment, 50-60g of sample was loaded in a ceramic boat. The temperature was ramped up with a ramping rate of 5 °C min^{-1} and maintained at the annealing temperature (200 °C and 400 °C) for different annealing times (6 hours, 12 hours, 24 hours and 48 hours). Hereafter, the samples were collected directly from the oven and cooled down to room temperature in air.

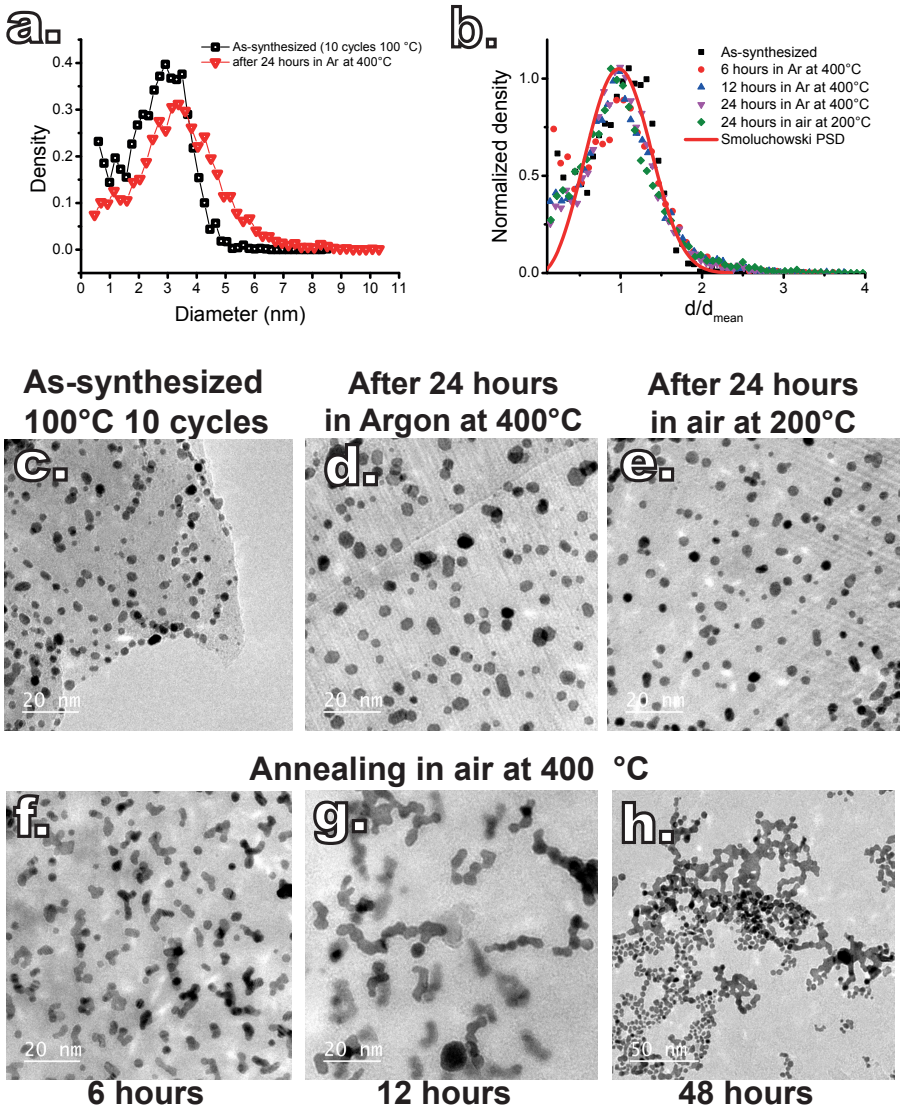

Figure S13: (a) PSD of the as-synthesized Pt/graphene after 10 cycles at 100°C compared with the PSD after 24 hours of annealing in argon at 400 °C. (b) PSDs of the as-synthesized Pt/graphene after 10 cycles at 100°C and after annealing at different temperatures and in different conditions rescaled with respect to their respective average diameter, compared with the Smoluchowski PSD. (c) TEM micrograph of the graphene nanoplatelets after 10 cycles at 100 °C. (d), (e), (f), (g), and (h) show the as-synthesized Pt/graphene of (c) after different annealing periods at different temperatures and in different atmospheres.

Dynamic Modeling

Here, we first elaborate on the modeling of the deposition process that allows for aggregation by single atoms and NP diffusion and coalescence (model(I)), and later we describe the modeling of the deposition process that allows for growth via single atoms diffusion and attachment and gas-phase-mediated ripening of the NPs via volatile PtO_2 (model(II)).

Model (I): deposition and irreversible aggregation by NP diffusion and coalescence

The nucleation and growth of nanoparticles is described by means of the Smoluchowski equation adjusted for compact 3D islands undergoing 2D diffusion and a time-dependent generation term accounting for deposition on both the substrate and the preexisting nanoparticles. The model thus describes the following physical picture:

- In each cycle a certain number of single atoms is generated on both the substrate surface and the preexisting NPs over the time scale τ_{rxn}, which is assumed to vary in the interval from 0 to the cycle time t_{cycle}. The single atoms diffuse over the substrate surface at a rate equal to $D_1(t)$. The meeting of two single atoms leads to the formation of a stable cluster (irreversible growth) or nanoparticle (NP). Once NPs are formed, single atoms can also attach to them (growth due to single-atom attachment). NPs diffuse over the substrate at a rate equal to D_k, where k is the size, i.e., number of atoms comprising the NP. The collision of an NP of size i with a cluster of size j leads to the irreversible and instantaneous formation of a NP of size $i + j$ (diffusion limited aggregation). In particular, only binary collisions are considered (low coverage hypothesis) and single atom detachment from NPs is not treated (no Ostwald ripening).

The model translates into the following population balance:

$$\frac{dn_1}{dt} = g_s(t) - n_1 \sum_{i=1}^{\infty} K_{1i} n_i \tag{5}$$

$$\frac{dn_k}{dt} = g_p(t)\left[n_{k-1}(k-1)a_{k-1} - n_k k a_k\right] + \frac{1}{2}\sum_{i+j=k} K_{ij} n_i n_j - n_k \sum_{i=1}^{\infty} K_{ki} n_i \tag{6}$$

where n_1 is the population of single atoms on the substrate (at/nm^2), n_k the population of NPs consisting of k atoms, K_{ij} the collision rate between entities of size i and j, a_k is the fraction of surface atoms in an NP of size k (i.e., dispersion), $g_s(t)$ is a time-dependent term accounting for the cyclic generation of mobile atoms on the substrate surface due to ALD reactions expressed in atoms per unit area and time, and, likewise, $g_p(t)$ accounts for direct deposition on NPs and is expressed in atoms per unit time per number of NP surface atoms (i.e., monolayers per unit time). Without loss of generality K_{ij} can be expressed as:[6–9]

$$K_{ij} = \sigma_i D_i + \sigma_j D_j \tag{7}$$

where σ_i and σ_j are referred to as capture numbers and account for geometric effects on the capture efficiency of species of size i and j, respectively; whereas, D_i and D_j are the 2D diffusion rates of the species i and j, respectively. The capture numbers are a function of the size and the spatial density of the NPs at any given time, and can be estimated from the analytical solution of the 2D diffusion problem in the neighborhood of a diffusing species of arbitrary size. Here, they were estimated in a self-consistent manner as described by Hubartt et al.,[8] by solving the following equation at each time step:

$$\sigma_i = \frac{2\pi r_i}{\xi} \frac{K_1(r_i/\xi)}{K_0(r_i/\xi)} \tag{8}$$

where r_i is the projected radius of the NP of size i, K_1 and K_0 are the modified Bessel functions of the second kind, and ξ is the diffusion length calculated estimated with the following equation:[8]

$$\xi^{-2} = \sum_{k=1}^{\infty} \sigma_k n_k \tag{9}$$

Given the 3D nature of the NPs, the projected diameter d_k ($2r_i$) is let:

$$d_k = \alpha k^{1/3} \tag{10}$$

where α is the NP shape factor, which is assumed to be constant over the whole size range. In the case of 3D compact islands undergoing 2D diffusion, the capture numbers are slowly varying functions of time and NPs size, and thus α, and constitute minor logarithmic corrections to the K_{ij} terms.[7,8,10] The diffusion rate D_k, on the other hand, can be a strong function of the NP size, and thus have a strong influence on the shape of the PSD. In fact, in the case of pure aggregation, if K_{ij} has the form $\sim (k_i^{-s} + k_j^{-s})$, where $s > 0$, it can be shown that the PSD exhibits self-similarity at long times and that, if rescaled with respect to the average size (number of atoms), it can be reduced to a sole function of the exponent s:[11–13]

$$f(x = j/j_{mean}) \sim \frac{(1+s)x^s}{\Gamma(1+s)} \exp[-(1+s)x] \tag{11}$$

The diffusion rate of 3D NPs has been widely observed to follow, indeed, a power law of the kind $D_k \sim k^{-s}$.[7–9,14–17] For this reason, here we let:

$$D_k = D_1(t)k^{-s} \tag{12}$$

where $D_1(t)$ is the diffusion rate of single atoms. However, the value of the exponent s can vary considerably and it is, in general, a poorly understood function of NP morphology, NP-substrate interaction, reacting atmosphere, and temperature. As such, here it is regarded as a fitting parameter. The dispersion a_k has been estimated by assuming the NPs to be metallic NPs with FCC close-packed structures, which is usually the case for supported Pt NPs, especially on carbon support, as already described elsewhere.[1,18]

The dynamic model (i.e., Eqs. (5), (6) together with (8) and (9)) was solved numerically by using an in-house code written and implemented in Matlab. The dynamic model was validated on three different levels: asymptotic behavior in case of pure aggregation (see

Figure S14), closure of the mass balance, and recovery of linear growth in case of sole deposition on NPs (see Figure S17b).
The functional form of $g_s(t)$, $g_p(t)$, and $D_1(t)$ is unknown a priori. However, their integral over a cycle time can be related to experimental quantities:

$$G_s = \int_{(n-1)\tau_{cycle}}^{n\tau_{cycle}} g_s(t)dt \tag{13}$$

$$G_p = \int_{(n-1)\tau_{cycle}}^{n\tau_{cycle}} g_p(t)dt \tag{14}$$

where G_s is the total number of single atoms deposited per unit of substrate area per cycle (at/nm^2/cycle), whereas G_s is the total number of atoms deposited on the NPs per number of NP surface atoms in one cycle (monolayers/cycle). Given this constraint $g_p(t)$ and $g_s(t)$ can assume different functional forms. For example, if we assume the generation term to follow an exponential decay:

$$g_p(t) = \frac{G_p}{\tau_{rxn}} \exp(-t/\tau_{rxn}),\ \tau_{rxn} << \tau_{cycle} \tag{15}$$

or assuming a constant generation during the reaction time, we have:

$$g_p(t) = \begin{cases} \frac{G_p}{\tau_{rxn}}t, & \text{for } t \leq \tau_{rxn} \\ 0, & \text{for } \tau_{rxn} < t < \tau_{cycle} \end{cases} \tag{16}$$

$D_1(t)$ is amenable to analogous formulations such as:

$$D_1(t) = \begin{cases} 0, & \text{for } t \leq \tau_0 \\ \frac{D_0\tau_{cycle}}{\tau_{cycle} - \tau_0 - \tau_{rxn}}[1 - e^{-(t-\tau_0)/\tau_{rxn}}], & \text{for } \tau_0 < t < \tau_{cycle} \end{cases} \tag{17}$$

and:

$$D_1(t) = 2D_0(1 - t/\tau_{cycle}) \tag{18}$$

or simply:

$$D_1(t) = \begin{cases} 0, & \text{for } t \leq \tau_0 \\ D_0\frac{\tau_{cycle}}{\tau_{cycle} - \tau_0}, & \text{for } \tau_0 < t < \tau_{cycle} \end{cases} \tag{19}$$

We studied the effect of several different functional forms for $g_s(t)$, $g_p(t)$, and $D_1(t)$ on the PSD for different values of s. Since for $s \neq 0$ the detailed balance of the single atom population has little to no effect on the shape of the PSD,[9] the exact time dependency of $D_1(t)$, $g_s(t)$, and $g_p(t)$ has little to no effect on the simulated PSD within the parameter space explored here, as opposed to the effect of varying s (see Figure S15). This is due to the dampening effect introduced by the coupling between the different NP populations prescribed by the first two terms in Eq. (6) on the fluctuations induced by time-dependent mobility and single-atom generation. Nonetheless, their average values over the cycle duration τ_{cycle} do affect the PSD, in particular:

$$\langle D_1 \rangle = \int_{(n-1)\tau_{cycle}}^{n\tau_{cycle}} D_1(t)dt \tag{20}$$

controls the total number of NPs per unit area, that is:

$$\sum_{k=2}^{\infty} n_k = s_p \tag{21}$$

whereas G_s and G_p determine the total number of deposited atoms in every p-th cycle, that is:

$$\sum_{k=1}^{\infty} n_k k = G_{tot}(p) \tag{22}$$

Accordingly, for each value of s, we varied G_s and G_p so as to match the experimental metal loading evolution, and $\langle D_1 \rangle$ to match the experimental average number of NPs per unit area, which was estimated to be $\sim 0.0025\,\mathrm{nm}^{-2}$ in the temperature range $100-200$°C and the cycle range $1-10$. By setting G_s equal to the loading after the first cycle ($\sim 0.12\,\mathrm{nm}^{-2}$) and G_p equal to the growth per cycle reported for flat substrates,[19–21] expressed in monolayers ($\sim$ 0.18 ML), we could reproduce the evolution of the metal loading with the number of cycles over a wide range of $\langle D_1 \rangle$ and s values (see Figure S16), and thus PSD shapes, consistently with the experimental observation that different deposition temperatures resulted in the same metal loading and yet different PSDs. The agreement between experimental and simulated PSDs has been quantified in terms of the sum of the squared errors (SSE) after rescaling the PSDs with respect to their respective average diameter, since by doing so the shape factor α cancels out, thus not affecting the agreement evaluation. As the shape factor α could not be estimated experimentally, it was assumed to be 0.35, that is, an NP consisting of 55 atoms has a projected diameter of 1.33 nm, as this value gave the best visual agreement when plotting the PSDs in terms of projected diameter.

In sum, since the agreement between simulated and experimental PSDs depended, *de facto*, on the sole parameter s, which is thus here regarded as the fitting parameter of the model, as G_p, G_s, and $\langle D_1 \rangle$ were determined independently. This procedure is analogous to the one employed by Kinosita[22] to study the growth of gold clusters on amorphous carbon, and more recently by Bell et al.[17] to study the size-dependent mobility of gold nano-clusters on chemically modified graphene.

Model (II): deposition, aggregation by surface diffusion of single atoms and gas-phase-mediated ripening via volatile PtO_2

To explore the effect of gas-phase-mediated Ostwald ripening we modified equation (5) and (6) to allow for the exchange of Pt atoms via volatile PtO_2(g) driven by the size-dependent stability of NPs (Gibbs-Thompson effect). To understand whether Ostwald ripening can account for the observed PSD evolution, we set the NP mobility to zero, i.e., $D_k = 0$ for $k \neq 1$. This model thus describes the following physical picture:

- In each cycle a certain number of single atoms is generated on both the substrate surface and the preexisting NPs over the time scale τ_{rxn}, which is assumed to vary in the interval from 0 to the cycle time t_{cycle}. The single atoms diffuse over the substrate surface at a rate equal to D_1. The meeting of two single atoms leads to the formation of a cluster or nanoparticle (NP). Once the NPs are formed, single atoms can attach to them (growth due to single-atom attachment). NPs can exchange single atoms in the form of volatile PtO_2 through the gas phase. The NPs are assumed in equilibrium with PtO_2. Since the equilibrium pressure of PtO_2 varies according to the Gibbs-Thompson equation, small particles grow smaller and disappear at expenses of larger ones.

The modeling of the exchange of volatile PtO_2 between Pt NPs is based on the recent work of Plessow and Abild-Pedersen,[23] which builds on the seminal work of Wynblatt and Gjostein.[24] In brief, the pressure p_k of PtO_2(g) in equilibrium with an NP of size k (number of atoms) is given by:

$$p_k = p_{O_2} \exp\left(\frac{-\Delta G_{form}(PtO_2) + A_{tot}(k)\gamma_{avg}/k}{k_b T}\right) \tag{23}$$

where p_{O_2} is the oxygen pressure, $\Delta G_{form}(PtO_2)$ is the Gibbs energy of formation of PtO_2(g), which is here taken as equal to -1.69 eV,[23] $A_{tot}(k)$ is the exposed area of the NP, γ_{avg} the average surface energy of the NP facets, k_b is the Boltzmann constant, and T is the temperature expressed in K. Accordingly, the number of PtO_2(g) molecules striking an NP of size k per unit of time is given by the kinetic theory of gases:

$$J_k A_k = \frac{S}{\sqrt{2\pi m_{PtO_2} k_b T}}(p_b - p_k)A_k \tag{24}$$

Where S is the sticking coefficient and p_b is the background pressure or mean-field pressure of PtO_2(g), which is generally different from p_k. In particular, an NP with $p_k = p_b$ neither grows nor shrinks and its radius is typically referred to as the "critical radius". Assuming steady-state and no loss of PtO_2, p_b is given by:

$$p_b = \frac{\sum_k A_k n_k p_k}{\sum A_k n_k} \tag{25}$$

where n_k is again the population of NPs of size k (nm^{-2}) For our simulations we have chosen the parameters used by Plessow and Abild-Pedersen.[23] In particular, we have taken $\gamma_{avg} = \gamma_{111} + \Delta_\gamma$ =130 meV/Å^2 - 55 meV/Å^2, and $S = 1$.

Given that the number of Pt atoms exchanged by an NP of size k with the vapor basin is:

$$\Delta_{atoms}(k) \simeq J_k A_k \Delta t \tag{26}$$

the population balance describing the evolution in time of the PSD consists of the following system of differential equations:

$$\frac{dn_1}{dt} = g_s(t) - n_1 \sum_{i=1}^{\infty} K_{1i} n_i \tag{27}$$

$$\frac{dn_2}{dt} = -g_p(t) n_k k a_k + n_1^2 K_{1,1} - n_1 K_{1,k} n_2 + 2 n_2 J_2 A_2 \tag{28}$$

if $p_b - p_k < 0$, then $J_k < 0$ (the NPs shrink) and:

$$\frac{dn_k}{dt} = g_p(t)\left[n_{k-1}(k-1)a_{k-1} - n_k k a_k\right] + n_1(K_{1,k-1}n_{k-1} - K_{1,k}n_k) + (n_k J_k A_k - n_{k+1} J_{k+1} A_{k+1}) \tag{29}$$

whereas if $p_b - p_k \geq 0$, then $J_k \geq 0$ (the NPs ripen) and:

$$\frac{dn_k}{dt} = g_p(t)\left[n_{k-1}(k-1)a_{k-1} - n_k k a_k\right] + n_1(K_{1,k-1}n_{k-1} - K_{1,k}n_k) + (n_{k-1} J_{k-1} A_{k-1} - n_k J_k A_k) \tag{30}$$

Lifshitz-Slyozov-Wagner (LSW) PSD

According to Lifshitz-Slyozov-Wagner (LSW) theory, the PSD of an ensemble of particles undergoing diffusion-limited Ostwald ripening approaches the following stationary self-similar PSD:[25,26]

$f(r/r_{cr}) = f(u) = (3^4 e/2^{5/3}) u^2 \exp[-1/(1-2u/3)]/[(u+3)^{7/3}(1.5-u)^{11/3}]$, if $0 < u < 1.5$
$f(r/r_{cr}) = 0$, otherwise

where $r_{cr} =< r >$.

Asymptotic behavior for the case of pure aggregation

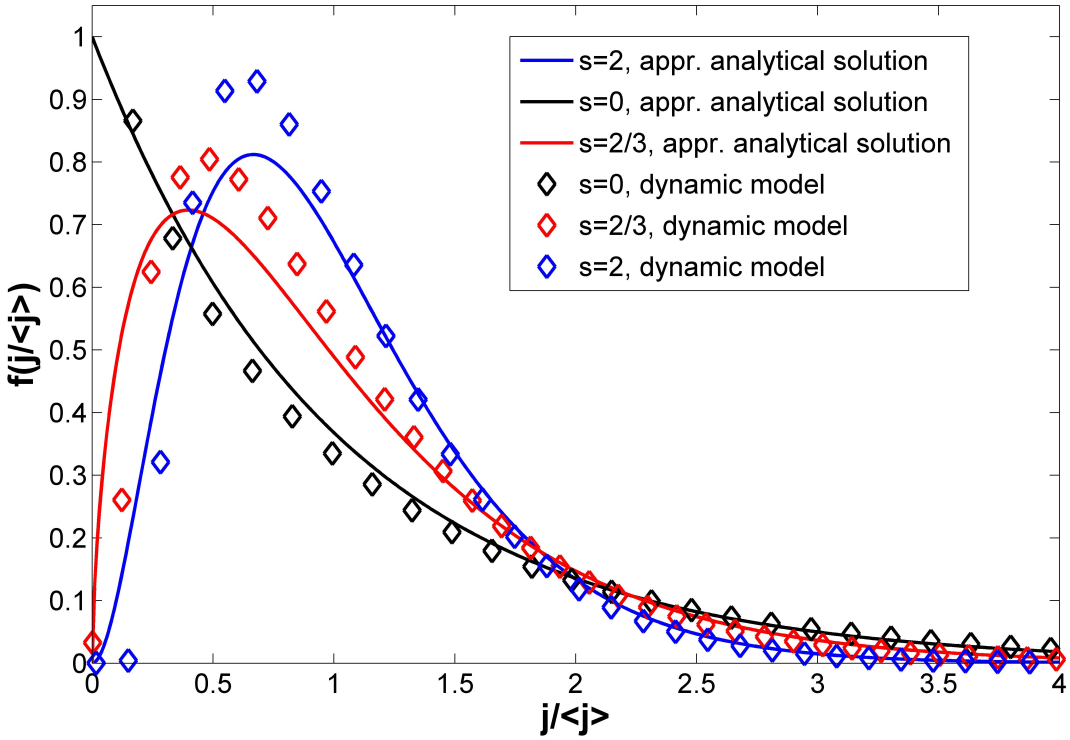

Figure S14: Long time solution to Eq. (6) in the case of pure aggregation ($g_s(t) = 0$ and $g_p(t) = 0$) as compared with the approximate analytical solution (11) for different values of s. The numerical solution is in satisfactory agreement with the from approximated solution. In particular, it deviates from it in the same fashion as reported by Sholl and Skodje.[12]

Parameter sensitivity of the aggregation model

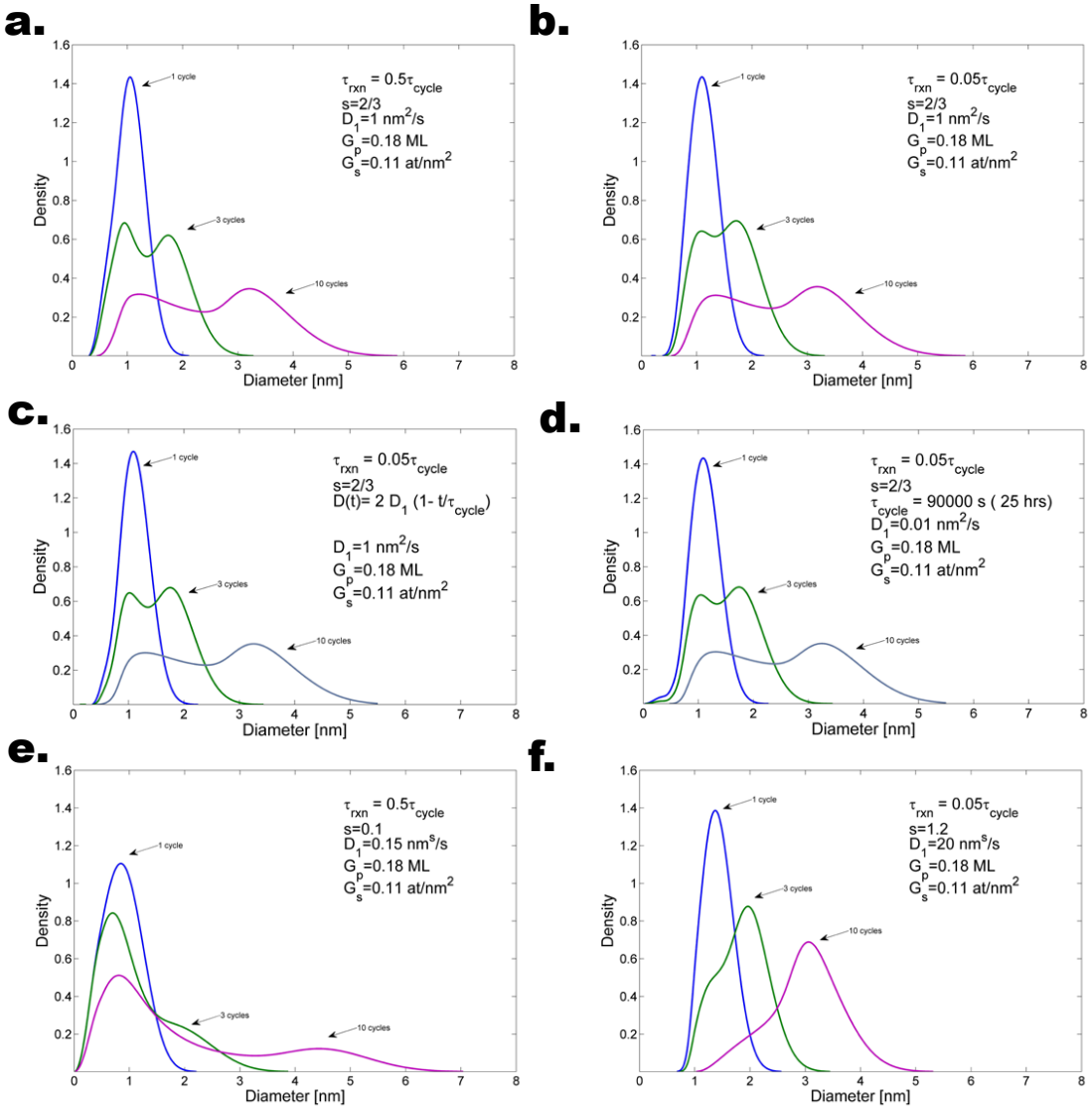

Figure S15: Simulated PSDs after 1, 3, and 10 cycles for the general case (deposition on both substrate and NPs + aggregation) for different values of s and τ_{rxn} (D_1 was varied to obtain the the same number of NPs in all cases), ($\tau_{cycle} = 900s$, unless specified otherwise). As shown in (a) and (b), a change of one order of magnitude in the value of τ_{rxn} has only a marginal effect on the PSD shape, in that higher values give a slightly higher peak on the small-size side. Furthermore increasing the cycle time by two orders of magnitude while reducing D_1 by two orders of magnitude (d) results in virtually the same PSD as in (b). Changing the functional form of $D_1(t)$ and $g_p(t)$ while keeping the constant the average value over the cycle time also has little to no effect on the PSD, for example (c) shows the case in which $D_1(t)$ varies linearly during the cycle time from a value of 2 nm^2/s to zero as opposed to having a constant value of 1 nm^2/s over the entire cycle time (b). However, changing the value of s from 0.1 (e) to 0.66 (a) and 1.2 (f) has a dramatic qualitative and quantitative effect on the shape of the PSD.

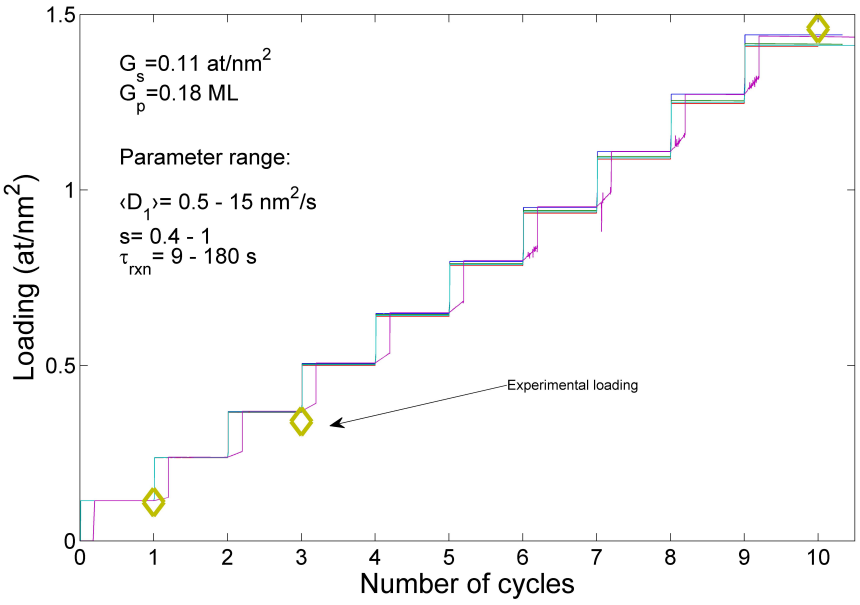

Figure S16: Simulated metal loading evolution for different values of D_1, s, and τ_{rxn} for G_s=0.11 at/nm^2 and $G_p = 0.18$ ML. ($\tau_{cycle} = 900$ s)

Case study: no aggregation, NP nucleation in the first cycle and subsequent growth due to exclusive deposition on NPs

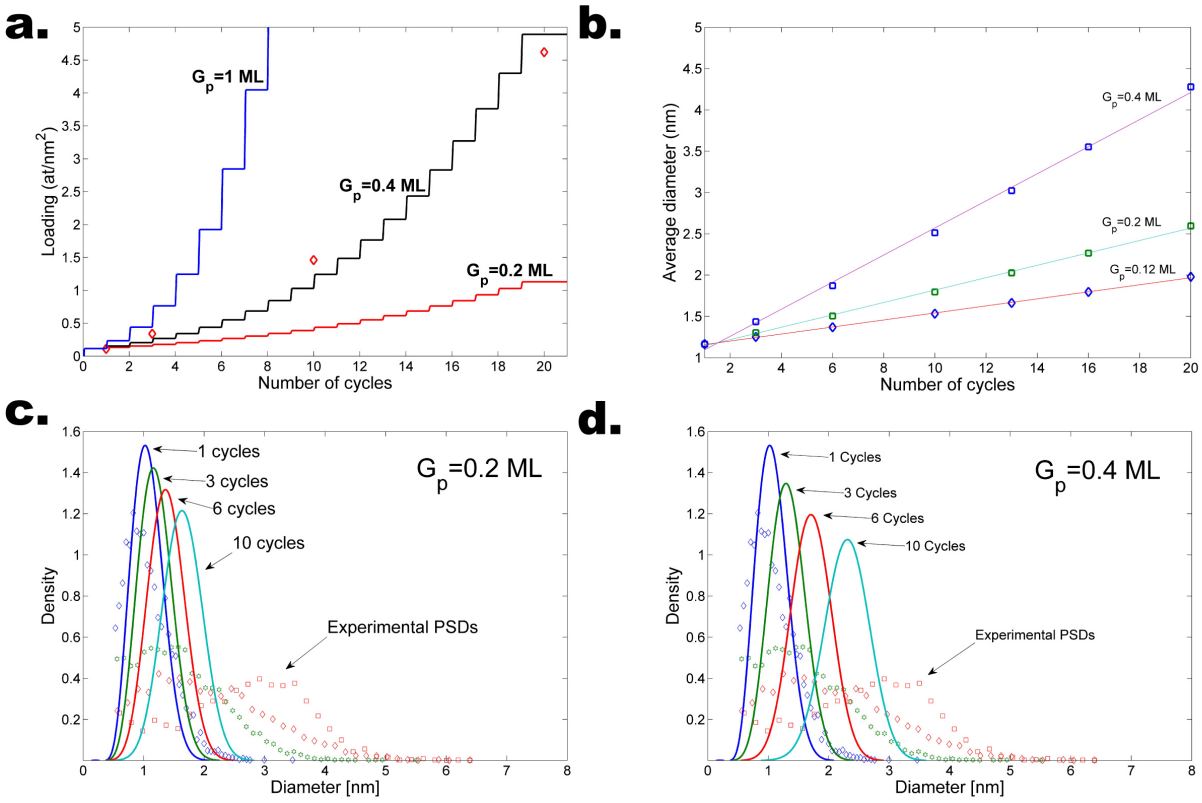

Figure S17: Simulation results for the case of NP nucleation in the first cycle followed by NP growth due to exclusive deposition on preexisting NPs (no aggregation, i.e., $D_k = 0$, and $G_s = 0$). (a) Simulated metal loading evolution (atoms per unit of substrate surface) for different values of G_p as compared to the experimental values (T=100 °C). (b) Evolution of the average diameter with the number of cycles for different values of G_p. (c) Simulated PSDs after 1, 3, 6, and 10 cycles for a G_p value of 0.2 ML and 0.4 ML (d) as compared with the experimental PSDs for a deposition temperature of 100 °C, ($\tau_{cycle} = 900s$). This scenario cannot give a qualitative description of the experimental PSD evolution. In particular, G_p values of about 0.2 ML, (i.e., the reported growth per cycle on planar Pt surfaces), drastically underestimate the metal loading after 10 cycles as well as the average size. G_p values of about 0.4 ML gives a fairly good fit to the metal evolution from 1 to 10 cycles. However, such a G_p still gives a poor description of the PSD and the average size evolution, apart from being an extremely high value compared to typical reported values for the growth per cycle of Pt ALD. Finally, in this case, it can be easily shown that the metal loading scales with the number of cycles i as $G_s^1 \prod_i (1 + \langle a_k^i \rangle G_p)^{i-1}$, where G_s^1 is the loading after the first cycle and $\langle a_k^i \rangle$ is the average fraction of surface atoms in the NPs at a given cycle.

Case study: growth via single atom deposition on both substrate and NPs, diffusion and attachment (no NP diffusion and coalescence)

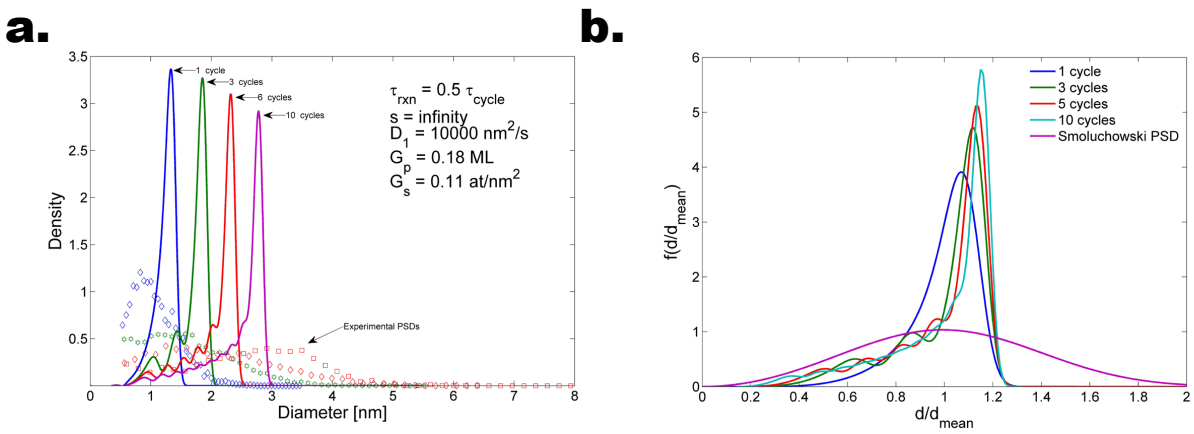

Figure S18: Simulated PSDs for the growth regime in which single atoms are the only mobile species, that is, $D_k = 0$ for $k \neq 0$. (a) Simulated PSDs after 1, 3, 6, and 10 cycles as opposed to the experimental PSDs for a deposition temperature of 100 °C (D_1 was varied to obtain an NP density of about 0.0025 nm^{-2}). (b) Evolution of the rescaled PSDs with the number of cycles (Smoluchowski PSD plotted for reference). ($\tau_{cycle} = 900s$)

Case study: growth via single atom deposition, diffusion and attachment (no NP diffusion and coalescence) and Ostwald ripening through PtO_2(g)

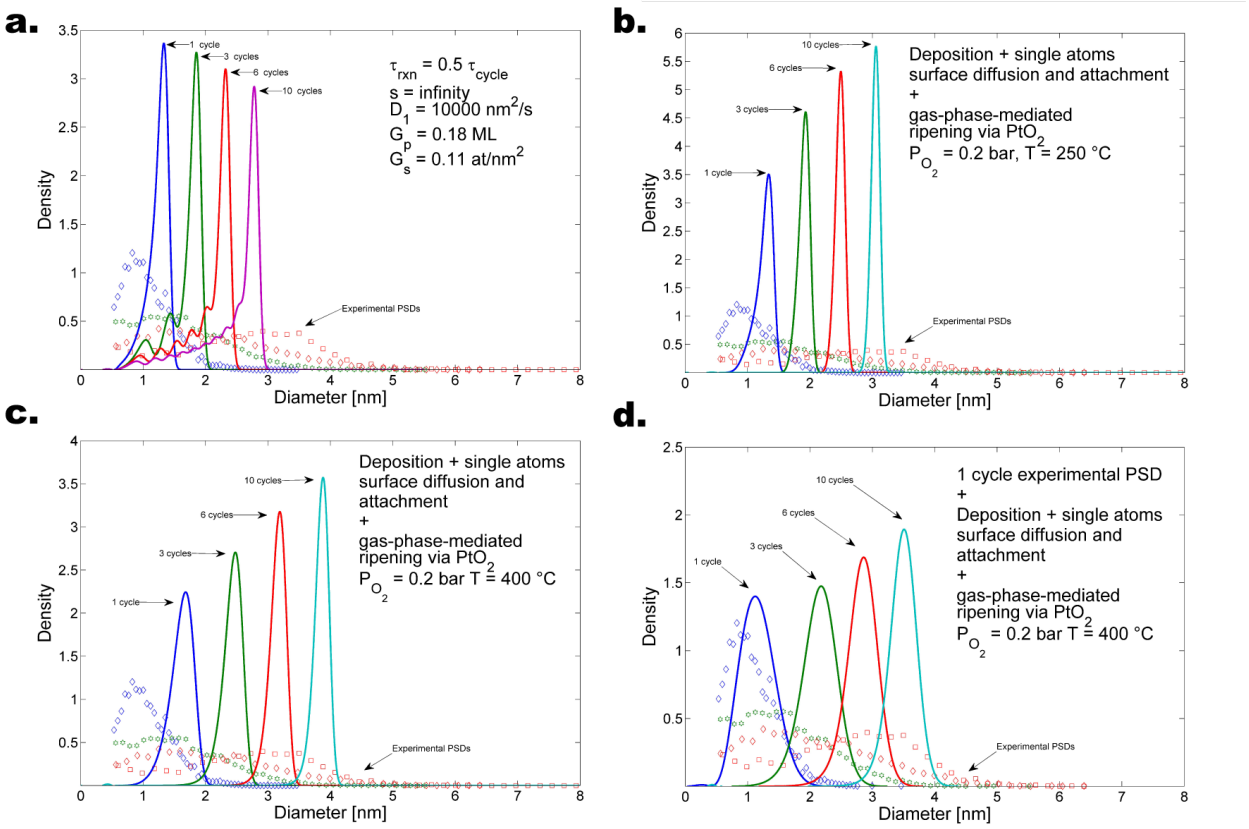

Figure S19: Simulated PSDs for the growth regime in which NPs can grow via gas-phase-mediated ripening through PtO_2(g), single atom deposition, diffusion and attachment ($D_k = 0$ for $k \neq 0$). (a) Shows the simulated PSDs for T=100 °C and $p_{O_2} = 0.2$ bar, where D_1, G_s, G_p, and τ_{cycle} are the same as in the ones used in the simulation of figure S18 (no NP diffusion and coalescence, and no Ostwald ripening). Up to 200 °C, the inclusion of Ostwald ripening has virtually no effect on the predicted PSDs. As compared to the base case (a) increasing the temperature above 200 °C (b) and (c) results in the disappearance of the tail on the small-sizes side and in a focusing (narrowing) of the PSD with increasing number of cycles. (d) Using the experimental right-skewed PSD as the initial condition also results in a focusing of the PSD with increasing number of cycles. Furthermore, the PSD, initially right-skewed, becomes symmetrical and slightly left-skewed.

Ostwald ripening during nucleation and growth: focusing and defocusing of the PSD, and its approach to the self-similar solution

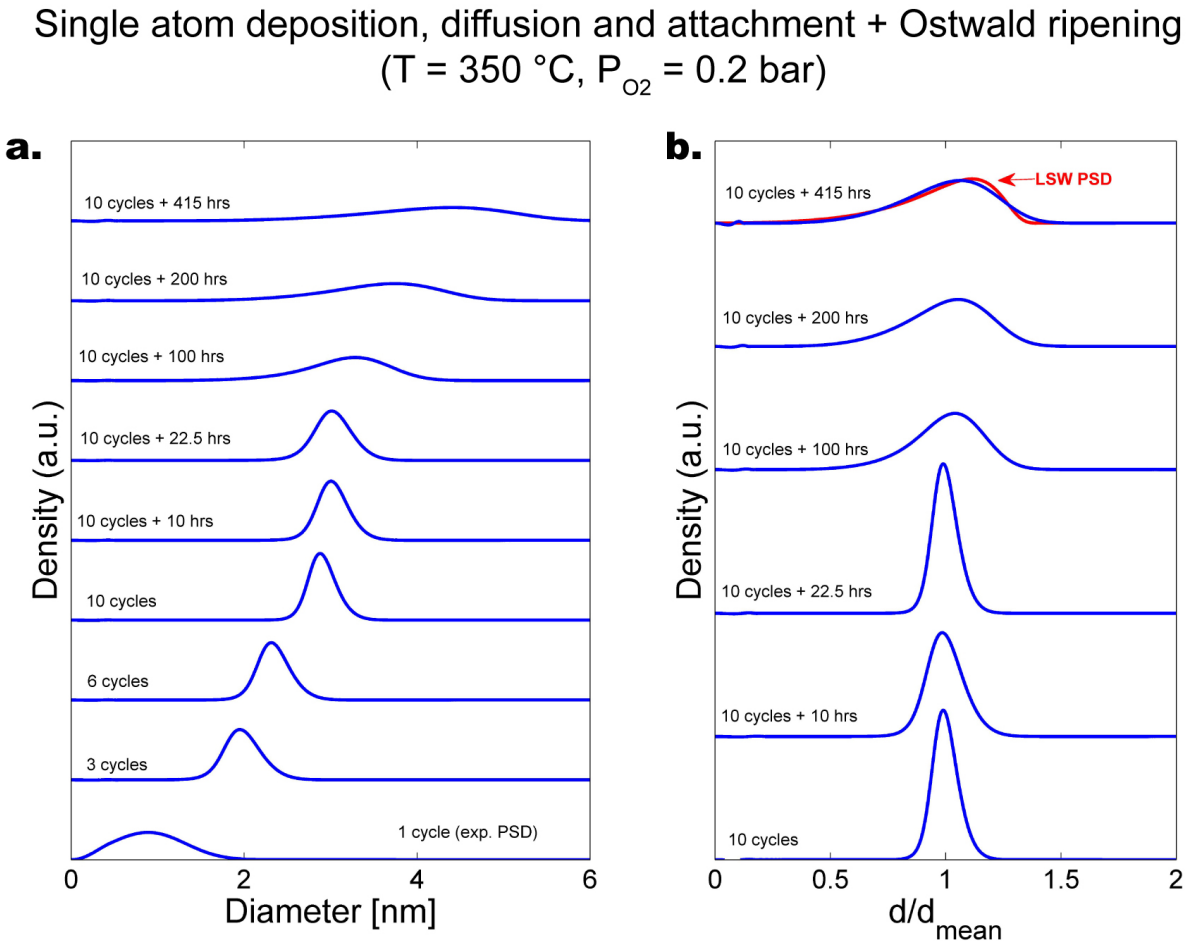

Figure S20: Simulated PSDs for the growth regime in which NPs can grow via gas-phase-mediated ripening through PtO_2(g), single atom deposition, diffusion and attachment ($D_k = 0$ for $k \neq 0$). D_1, G_s, G_p, and τ_{cycle} are the same as in the ones used in the simulations of figure S18 and S19. (a) Shows the evolution of the PSD with the number of cycles and subsequent annealing (no further deposition) using the experimental right-skewed PSD of figure S19d as the initial condition. (b) Shows the evolution of the PSD rescaled with respect to the average diameter during the annealing period and thus its approach to the self-similar solution. The latter is fairly close to the stationary PSD predicted by the Lifshitz-Slyozov-Wagner (LSW) theory for diffusion-limited ripening. In particular, the predicted stationary PSD is slightly more symmetric than the LSW PSD. Such discrepancy is ascribable to the fact that LSW theory is based on only the first two terms of the expansion of the Gibbs-Thompson equation, whereas our treatment does not rely on such simplification.[16,25]

Ostwald ripening: focusing and defocusing of an initial bimodal PSD, and its approach to the self-similar solution

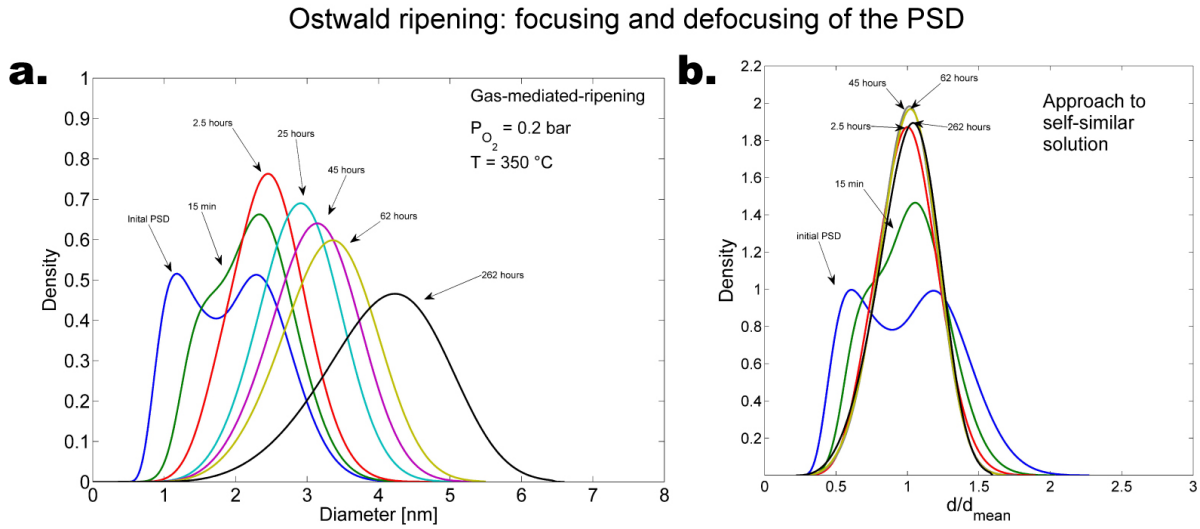

Figure S21: Simulated evolution of an initially bimodal PSD in case of pure Ostwald ripening (no deposition, no NP diffusion and coalescence). The initial PSD has been obtained by simulating 5 cycles using the model allowing for NP diffusion and coalescence and $s = 0.8$. This simulation shows how Ostwald ripening can give rise to an initial focusing (narrowing) of the PSD followed by a gradual defocusing (broadening) when the initial distribution is broader than the stationary PSD. In other words, Ostwald ripening does not always result into a broadening of the PSD.[25]

References

(1) Bui, H. V.; Grillo, F.; Helmer, R.; Goulas, A.; van Ommen, J. R. Controlled Growth of Palladium Nanoparticles on Graphene Nanoplatelets via Scalable Atmospheric Pressure Atomic Layer Deposition. *J. Phys. Chem. C* **2016**, *120*, 8832–8840.

(2) Puurunen, R. L. Surface chemistry of atomic layer deposition: A case study for the trimethylaluminum/water process. *J. Appl. Phys.* **2005**, *97*, 121301.

(3) Poole, C. P.; Jones, F. J.; Owens, F. J. *Introduction to Nanotechnology*; John Wiley & Sons, Inc.: New York, NY, USA, 2003.

(4) Montejano-Carrizales, J.; Aguilera-Granja, F.; Morán-López, J. Direct Enumeration of the Geometrical Characteristics of Clusters. *Nanostructured Materials* **1997**, *8*, 269 – 287.

(5) Fritsche, H.-G.; Benfield, R. Exact analytical formulae for mean coordination numbers in clusters. *Zeitschrift fur Physik D Atoms, Molecules and Clusters* **1993**, *26*, 15–17.

(6) Venables, J. A.; Spiller, G. D. T.; Hanbucken, M. Nucleation and growth of thin films. *Reports on Progress in Physics* **1984**, *47*, 399–459.

(7) Kryukov, Y. A.; Amar, J. G. Effects of cluster diffusion on the island density and size distribution in submonolayer island growth. *Physical Review E* **2011**, *83*.

(8) Hubartt, B. C.; Kryukov, Y. A.; Amar, J. G. Rate-equation approach to irreversible island growth with cluster diffusion. *Physical Review E* **2011**, *84*.

(9) Vicanek, M.; Ghoniem, N. The effects of mobility coalescence on the evolution of surface atomic clusters. *Thin Solid Films* **1992**, *207*, 90–97.

(10) Ruckenstein, E. Growth kinetics and the size distributions of supported metal crystallites. *Journal of Catalysis* **1973**, *29*, 224–245.

(11) Kandel, D. Selection of the Scaling Solution in a Cluster Coalescence Model. *Physical Review Letters* **1997**, *79*, 4238–4241.

(12) Sholl, D. S.; Skodje, R. T. Late-stage coarsening of adlayers by dynamic cluster coalescence. *Physica A: Statistical Mechanics and its Applications* **1996**, *231*, 631–647.

(13) Botet, R.; Jullien, R. Size distribution of clusters in irreversible kinetic aggregation. *Journal of Physics A: Mathematical and General* **1984**, *17*, 2517–2530.

(14) Jensen, P. Growth of nanostructures by cluster deposition: Experiments and simple models. *Reviews of Modern Physics* **1999**, *71*, 1695–1735.

(15) Winkler, K.; Wojciechowski, T.; Liszewska, M.; Górecka, E.; Fiałkowski, M. Morphological changes of gold nanoparticles due to adsorption onto silicon substrate and oxygen plasma treatment. *RSC Adv.* **2014**, *4*, 12729–12736.

(16) Jak, M.; Konstapel, C.; van Kreuningen, A.; Verhoeven, J.; Frenken, J. Scanning tunnelling microscopy study of the growth of small palladium particles on TiO2(110). *Surface Science* **2000**, *457*, 295–310.

(17) Bell, G. R.; Dawson, P. M.; Pandey, P. A.; Wilson, N. R.; Mulheran, P. A. Size-dependent mobility of gold nano-clusters during growth on chemically modified graphene. *APL Mater.* **2014**, *2*, 012109.

(18) Agostini, G.; Pellegrini, R.; Leofanti, G.; Bertinetti, L.; Bertarione, S.; Groppo, E.; Zecchina, A.; Lamberti, C. Determination of the Particle Size, Available Surface Area, and Nature of Exposed Sites for Silica-Alumina-Supported Pd Nanoparticles: A Multitechnical Approach. *J. Phys. Chem. C* **2009**, *113*, 10485–10492.

(19) Aaltonen, T.; Ritala, M.; Sajavaara, T.; Keinonen, J.; Leskela, M. Atomic Layer Deposition of Platinum Thin Films. *Chemistry of Materials* **2003**, *15*, 1924–1928.

(20) Mackus, A. J. M.; Verheijen, M. A.; Leick, N.; Bol, A. A.; Kessels, W. M. M. Influence of Oxygen Exposure on the Nucleation of Platinum Atomic Layer Deposition: Consequences for Film Growth, Nanopatterning, and Nanoparticle Synthesis. *Chemistry of Materials* **2013**, *25*, 1905–1911.

(21) Mackus, A. J. M.; Weber, M. J.; Thissen, N. F. W.; Garcia-Alonso, D.; Vervuurt, R. H. J.; Assali, S.; Bol, A. A.; Verheijen, M. A.; Kessels, W. M. M. Atomic layer deposition of Pd and Pt nanoparticles for catalysis: on the mechanisms of nanoparticle formation. *Nanotechnology* **2015**, *27*, 034001.

(22) Kinosita, K. Mobility of small clusters on the substrate surface. *Thin Solid Films* **1981**, *85*, 223 – 238.

(23) Plessow, P. N.; Abild-Pedersen, F. Sintering of Pt Nanoparticles via Volatile PtO2: Simulation and Comparison with Experiments. *ACS Catalysis* **2016**, *6*, 7098–7108.

(24) Wynblatt, P.; Gjostein, N. Supported metal crystallites. *Progress in Solid State Chemistry* **1975**, *9*, 21–58.

(25) Talapin, D. V.; Rogach, A. L.; Haase, M.; Weller, H. Evolution of an Ensemble of Nanoparticles in a Colloidal Solution: Theoretical Study. *The Journal of Physical Chemistry B* **2001**, *105*, 12278–12285.

(26) Woehl, T. J.; Park, C.; Evans, J. E.; Arslan, I.; Ristenpart, W. D.; Browning, N. D. Direct Observation of Aggregative Nanoparticle Growth: Kinetic Modeling of the Size Distribution and Growth Rate. *Nano Letters* **2014**, *14*, 373–378.